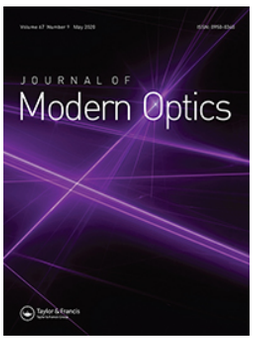

Journal of Modern Optics

ISSN: (Print) (Online) Journal homepage: https://www.tandfonline.com/loi/tmop20

Convergent Born series improves the accuracy of numerical solution of time-independent photoacoustic wave equation

Anuj Kaushik , Phaneendra K. Yalavarthy & Ratan K. Saha

To cite this article: Anuj Kaushik , Phaneendra K. Yalavarthy & Ratan K. Saha (2020) Convergent Born series improves the accuracy of numerical solution of time-independent photoacoustic wave equation, Journal of Modern Optics, 67:9, 849-855, DOI: 10.1080/09500340.2020.1777334

To link to this article: https://doi.org/10.1080/09500340.2020.1777334

Published online: 15 Jun 2020.

JOURNAL OF MODERN OPTICS
2020, VOL. 67, NO. 9, 849–855
https://doi.org/10.1080/09500340.2020.1777334

Taylor & Francis
Taylor & Francis Group

Convergent Born series improves the accuracy of numerical solution of time-independent photoacoustic wave equation

Anuj Kaushik[a], Phaneendra K. Yalavarthy[b] and Ratan K. Saha[a]

[a]Department of Applied Sciences, Indian Institute of Information Technology, Allahabad, India; [b]Department of Computational and Data Sciences, Indian Institute of Science, Bangalore, India

ABSTRACT

This work presents two variants of Born-series methods, for the first time, providing a numerical solution to the time-independent photoacoustic wave equation. These methods are effective in providing accurate solution even when there is a mismatch in speed-of-sound between the source and the ambient region. The traditional Born-series (TBS) and convergent Born-series (CBS) methods have been systematically compared for a test imaging case. The solution was computed keeping speed-of-sound outside the source as constant (1500 m/s) and varying the same quantity from 1950 to 1200 m/s inside the source (a disc with 5 μm radius) over a large frequency band (7–2000 MHz). The TBS method fails to converge when the variation in the speed-of-sound is approximately $>$ 22% or $<$ −11%. The CBS method provides the required robust numerical solution even in case of mismatch in speed-of-sound in various regions of imaging domain.

ARTICLE HISTORY
Received 22 April 2020
Accepted 27 May 2020

KEYWORDS
Time-independent photoacoustic wave equation; convergent Born series; traditional Born series; numerical solution; speed-of-sound mismatch

1. Introduction

The time-independent Photoacoustic (PA) wave equation can be treated as an inhomogeneous Helmholtz equation, whose solution has applications in various fields of science, engineering, and medicine. The range of applications span from seismology to electron scattering [1]. For simple and regular geometries like spherical and infinite cylinder, the analytical solutions are readily available in the literature [2,3]. For irregular geometries, only approximate numerical solution can be computed, an example of such numerical schemes include finite difference time domain, pseudospectral time domain and finite-element methods. These methods either provide a numerical solution for the second-order wave equation or for a set of first-order differential equations.

The other class of methods solve integral equations using Green's function approach [4], with traditional Born-series (TBS) method being the widely used especially for the inhomogeneous Hemlholtz equation. The TBS converges for small particles and relatively small scattering potential problems. The TBS method is not effective if the particle size or scattering potential is large. Recent work by Osnabrugge et al. [5] addressed this issue by introducing a pre-conditioner into the TBS expression and called it as convergent Born-series (CBS) method. It has been shown that CBS method converges for arbitrarily large media, in turn providing accurate solution to the inhomogeneous Helmholtz equation [5,6].

The time-independent PA wave equation with a mismatch of the speed-of-sound between the source region and surrounding media can be considered as inhomogeneous Helmholtz equation. As mentioned earlier, for simple geometries exact analytical solutions are available [7]. The solution to time-dependent PA wave equation for an acoustically inhomogeneous media can be computed using k-Wave toolbox which implements pseudospectral method [8]. Natalie et al. [9,10] proposed a transfer function approach to solve inhomogeneous PA wave equation and also performed image reconstruction. They used non-delta input waveform (unlike Green's function approach) and showed that the reconstruction of initial pressure can be improved significantly. Further, previous works involving Green's function approach did not consider acoustic inhomogeneity of the source [11,12]. The existing solutions may not be accurate, for example, in the computation of PA wave field from a red blood cell (RBC) in which speed-of-sound mismatch with respect to saline water is greater than 10%.

This work demonstrates that the CBS method can be extended to solve time-independent inhomogeneous PA wave equation for arbitrary large source region with

CONTACT Ratan K. Saha ratank.saha@iiita.ac.in Department of Applied Sciences, Indian Institute of Information Technology, Allahabad, 211015, India

mismatch in the speed-of-sound. This is also the first time the Born-series methods have been applied in providing solution to photoacoustic wave equation and shown to be effective compared to the existing methods. The results from the TBS and CBS methods have been compared with analytical solutions in order to evaluate their performance. The analytical (exact) solution have been obtained for a circular source region (typical RBC shape), and its speed-of-sound has been varied from 30% to −20% in comparison to the ambient medium. The numerical results presented in this work show that the CBS method has a greater validity and provides a more accurate solution than the existing TBS method, making it universally applicable.

2. Material and methods

Consider that the PA waves are generated by an acoustically inhomogeneous light absorbing region. The well-known time-independent PA wave equation in this case can be written as [7],

$$\nabla^2\psi(\mathbf{r}) + k_s^2\psi(\mathbf{r}) = \frac{\mathrm{i}\omega\mu\beta I_0}{C_P}, \text{ within the source,} \quad (1a)$$

$$\nabla^2\psi(\mathbf{r}) + k_f^2\psi(\mathbf{r}) = 0, \text{ in the surrounding medium,} \quad (1b)$$

where μ, β, and C_P are the optical absorption coefficient, isobaric thermal expansion coefficient, and specific heat for the absorbing region, respectively; ω and I_0 are the modulation frequency and the intensity of the incident light beam, respectively [7]. Here, k_s and k_f indicate the wave numbers inside and outside the PA source, respectively. The analytical solution to Equation (1) can be obtained easily for regular shapes (e.g. sphere, infinite cylinder, layer, etc.) by solving the above equations and by demanding continuity of the pressure and normal component of the particle velocity at the boundary [7]. This is referred to as the exact method, which works for any inhomogeneity (without size restriction) of arbitrary strength. The PA field at a point $\mathbf{r}$ (outside the source) for an infinite cylinder of radius a becomes [7],

$$\psi_{\mathrm{ex}}(\mathbf{r}) = A\left[\frac{J_1(k_s a)H_0^1(k_f r)}{k_s a[J_1(k_s a)H_0^1(k_f a) - \hat{\rho}\hat{c}J_0(k_s a)H_1^1(k_f a)]}\right]. \quad (2)$$

Here, $A = \mathrm{i}\mu\beta I_o v_s a/C_p$, J and H^1 represent the Bessel function and the Hankel function of first kind, respectively. The subscripts 0 and 1 dictate the order of each function. In the above equation, $\hat{\rho} = \rho_s/\rho_f$ and $\hat{c} = v_s/v_f$ are the dimensionless ratios for the density and speed-of-sound inside the disc relative to those outside the disc, respectively. The subscript ex represents the exact solution.

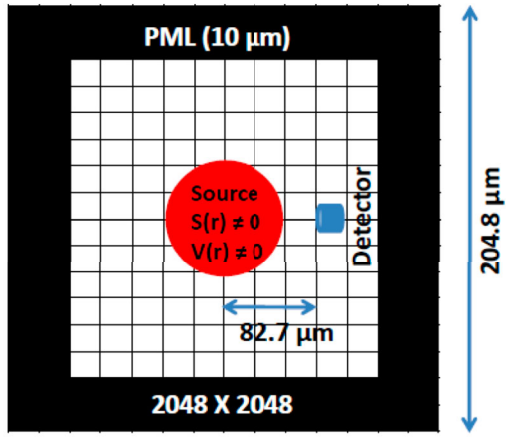

Figure 1. Schematic diagram of the PA source and surrounding medium for computation of photoacoustic field. PML stands for perfectly matched layer.

The PA wave equation as given in Equation (1) can be rewritten in a combined form as [5],

$$\nabla^2\psi(\mathbf{r}) + (k_f^2 + \mathrm{i}\epsilon)\psi(\mathbf{r}) = -S(\mathbf{r}) - V(\mathbf{r})\psi(\mathbf{r}), \quad (3)$$

where ϵ is infinitesimally small and

$$V(\mathbf{r}) = \begin{cases} k_s^2 - k_f^2 - \mathrm{i}\epsilon, & \text{if } |\mathbf{r}| \le \mathbf{a} \\ -\mathrm{i}\epsilon, & \text{if } |\mathbf{r}| > \mathbf{a} \end{cases} \quad (4)$$

similarly,

$$S(\mathbf{r}) = \begin{cases} -\frac{\mathrm{i}\mu\beta I_o\omega}{C_p}, & \text{if } |\mathbf{r}| \le \mathbf{a} \\ 0. & \text{if } |\mathbf{r}| > \mathbf{a} \end{cases} \quad (5)$$

with $S(\mathbf{r})$ being the source term and $V(\mathbf{r})$ behaves as the scattering potential in Equation (3). A representative schematic of the PA source along with surrounding media that was utilized in this work is shown in Figure 1.

Using Green's function method, the solution to Equation (3) can be written as [4,5],

$$\psi(\mathbf{r}) = \int g(\mathbf{r}|\mathbf{r}_0)[V(\mathbf{r}_0)\psi(\mathbf{r}_0) + S(\mathbf{r}_0)]d^3\mathbf{r}_0, \quad (6)$$

where Green's function $g(\mathbf{r}|\mathbf{r}_0)$ is defined as the solution to,

$$\nabla^2 g(\mathbf{r}|\mathbf{r}_0) + (k_f^2 + \mathrm{i}\epsilon)g(\mathbf{r}|\mathbf{r}_0) = -\delta(\mathbf{r} - \mathbf{r}_0), \quad (7)$$

δ is the Dirac delta function. It may be noted that in the frequency domain, Green's function in terms of Fourier

transformed coordinates ($\mathbf{p}$) can be expressed as,

$$\tilde{g}(\mathbf{p}) = \frac{1}{(|\mathbf{p}|^2 - k_f^2 - \mathrm{i}\epsilon)}, \tag{8}$$

which is useful in finding the actual functional form of $g(\mathbf{r}|\mathbf{r}_0)$. For example, Green's function in the far field in two and three dimensions for lossy unbounded medium becomes,

$$g(\mathbf{r}|\mathbf{r}_0) \approx \frac{\mathrm{i}}{4}\left(\frac{2}{\pi\sqrt{k_f^2 + \mathrm{i}\epsilon}|\mathbf{r}|}\right)^{1/2} \mathrm{e}^{\mathrm{i}\left(\sqrt{k_f^2+\mathrm{i}\epsilon}|\mathbf{r}-\mathbf{r}_0|-\pi/4\right)}, \tag{9}$$

and

$$g(\mathbf{r}|\mathbf{r}_0) \approx \frac{\mathrm{e}^{\mathrm{i}\sqrt{k_f^2+\mathrm{i}\epsilon}|\mathbf{r}-\mathbf{r}_0|}}{4\pi|\mathbf{r}|}, \tag{10}$$

respectively. Equations (9) and (10) demonstrate that Green's function in both cases decays exponentially with distance for finite ϵ, which localizes the function and also makes its total energy is finite [5]. The convolution sum presented in Equation (6) can be expressed in the matrix form yielding,

$$\psi = GV\psi + GS, \tag{11}$$

where $G = F^{-1}\tilde{g}(\mathbf{p})F$, with F and F^{-1} as the forward and inverse Fourier transform operators, respectively. The TBS method can be arrived by expanding Equation (11) recursively as,

$$\psi_{\mathrm{TBS}} = [1 + GV + GVGV + \cdots]GS. \tag{12}$$

The above infinite series converges only when GV is less than unity [5]. The TBS method has been found to be efficient only for solving the Helmholtz equation for the small objects having weak scattering potential.

Multiplying by a pre-conditioner (γ) on both sides of Equation (11) results in [5],

$$\gamma\psi = \gamma GV\psi + \gamma GS. \tag{13}$$

This pre-conditioner helps the TBS to converge for large structures [5], which forms the basis for CBS. Then Equation (13) after rearrangement of terms reduces to,

$$\psi_{\mathrm{CBS}} = M\psi_{\mathrm{CBS}} + \gamma GS, \tag{14}$$

where $M = \gamma GV - \gamma + 1$. As in the previous case, an infinite series can be obtained by recursive expansion of Equation (14) as,

$$\psi_{\mathrm{CBS}} = [1 + M + M^2 + \cdots]\gamma GS. \tag{15}$$

Even here, the above equation converges only if $M < 1$. Moreover, it converges for all structures if one chooses [5],

$$\gamma = \frac{\mathrm{i}}{\epsilon}V(\mathbf{r}), \tag{16}$$

and

$$\epsilon \geq \max|k_s^2 - k_f^2|. \tag{17}$$

In this work, the pressure field generated by a circular solid disc has been computed by employing the proposed TBS and CBS methods. Further, the computed results have been systematically compared to the exact solution.

3. Computation of pressure field

The numerical experiments in this work were restricted to two dimensions to limit the execution time. The algorithm developed for the implementation of the TBS and CBS schemes is summarized in Algorithm 1. The two-dimensional computational grid was taken as 2048×2048 with a pixel size of 100 nm (see Figure 1). A perfectly matched layer (PML) of 100 grid points was utilized to attenuate the propagating waves, which significantly reduce amplitudes of the reflected waves arising from the boundaries. Essentially, waves in the boundary layer were dampened exponentially with decay constant $\sqrt{\epsilon}$. This condition may be implemented in practice by defining a mask (*AtnMsk*) as,

$$AtnMsk(\mathbf{r}) = \begin{cases} \exp(-\sqrt{\epsilon}|\mathbf{r}|), & \text{if } |\mathbf{r}| \text{ lies within the PML} \\ 1 & \text{otherwise.} \end{cases} \tag{18}$$

Further, the convolution sums in Equations (11) and (14) have been evaluated using a fast Fourier transform which inherently implements the periodic boundary conditions. The above step is important to wrap around the boundaries and to obtain accurate estimates of the PA field.

A circular disc with $a = 5\,\mu$m was placed at the centre. The exact method provided a closed-form solution for such a disc (Equation (2)). The density of the medium inside the PA source was considered to be the same as that of the outside, $\rho_s = \rho_f = 1000\,\mathrm{kg/m^3}$. The speed-of-sound of the ambient medium was fixed at $v_f = 1500$ m/s. The numerical values of density and speed-of-sound of saline water (which is a tissue mimicking medium) at 27°C are close to these values [11,12]. The

Algorithm 1 Algorithm for computation of the pressure field using proposed TBS and CBS methods.

Input: amp; Size of the computational domain ($N_y \times N_x$), grid size ($dx = dy$) and
amp; frequency array (f)
amp; Physical parameters (I_0, μ, β, C_P, v_s, v_f, a)
Output: amp; Steady-state pressure field, ψ_{n+1}
Step 1: amp; **for** $m = 1, 2, ...,$ length of f do Steps 2-6
Step 2 amp; Calculate ω, k_s, k_f, and ϵ
Step 3: amp; Computation of spatial distribution of various parameters within the
amp; simulation domain
amp; **for** $j = 1, 2, ..., N_y$ do step A
A. amp; **for** $l = 1, 2, ..., N_x$ do steps i-iv
i. amp; $k_x \leftarrow 2\pi \frac{l-\frac{N_x}{2}-1}{N_x dx}$
ii. amp; $k_y \leftarrow 2\pi \frac{j-\frac{N_y}{2}-1}{N_y dy}$
iii. amp; $|\mathbf{p}| \leftarrow \sqrt{k_x^2 + k_y^2}$
iv. amp; Evaluate V, S, $\tilde{g}$, γ and *AtnMsk* using Equations (4), (5), (8), (16) and
amp; (18), respectively
Step 4: amp; Initialization of pressure field
amp; ψ_n for the TBS and CBS as given in Equations (21) and (22), respectively
Step 5: amp; Determination of pressure field
amp; **for** $n = 1, ..., 2000$ do steps i-vii
i. amp; Estimate ψ_{n+1} for the TBS and CBS employing Equations (19) and (20),
amp; respectively
ii. amp; Calculate Total error from Equation (23)
iii. amp; **if** Total error $\leq 10^{-4}$
iv. amp; **break**
v. amp; **else**
vi. amp; $\psi_n \leftarrow AtnMsk\ \psi_{n+1}$
vii. amp;amp; **end**
Step 6: amp; Store steady-state pressure field, ψ_{n+1}

speed-of-sound within the source was varied as v_s = 1950, 1800, 1650, 1500, 1350, and 1200 m/s. Therefore, mismatch of speed-of-sound has been within 30% to −20% with respect to that of the ambient medium. The performance of the TBS and CBS methods with respect to the exact method have been evaluated under these conditions. Optical and thermo-mechanical parameters for the PA source were set to unity ($I_0 = 1$, $\mu = 1$, $\beta = 1$, $C_p = 1$) to limit the amplitude of the PA field without affecting its spectral features [11,13]. A point detector was placed at a distance of 82.7 μm from the centre to record pressure data. All computations were performed in Matlab environment and executed in a high performance virtual machine (CentOS, Intel Core Processor (Broadwell, IBRS) working at 2.19 GHz, 128 GB RAM, 40 Cores).

The PA fields were computed for 274 frequency points ranging from 7.3 to 2000 MHz with an increment of 7.3 MHz for the exact, TBS, and CBS methods. The pressure data for the TBS and CBS algorithms were computed in the following manner,

$$\psi_{\mathrm{TBS}_{n+1}}(\mathbf{r}) = \mathrm{ifft}_2[\tilde{g}(\mathbf{p})\mathrm{fft}_2[V(\mathbf{r})\psi_{\mathrm{TBS}_n}(\mathbf{r}) + S(\mathbf{r})]], \tag{19}$$

and

$$\psi_{\mathrm{CBS}_{n+1}}(\mathbf{r}) = \psi_{\mathrm{CBS}_n}(\mathbf{r}) - (i/\epsilon)V(\mathbf{r})(\psi_{\mathrm{CBS}_n}(\mathbf{r}) - \mathrm{ifft}_2[\tilde{g}(\mathbf{p})\mathrm{fft}_2[V(\mathbf{r})\psi_{\mathrm{CBS}_n}(\mathbf{r}) + S(\mathbf{r})]]), \tag{20}$$

where n is the iteration number and all multiplications were performed element wise; the notations fft_2 and ifft_2 state the forward and inverse fast Fourier transforms in two dimensions. For each frequency, at first $V(\mathbf{r})$ and $S(\mathbf{r})$ were computed as defined in Equations (4) and (5), respectively. Note that ϵ was set to be $0.8k_f^2$. Green's function was also evaluated for each grid point in the

frequency space. Initial pressure values were taken as,

$$\psi_{\mathrm{TBS}_0}(\mathbf{r}) = \mathrm{ifft}_2[\tilde{g}(\mathbf{p})\mathrm{fft}_2 S(\mathbf{r})], \tag{21}$$

and

$$\psi_{\mathrm{CBS}_0}(\mathbf{r}) = \gamma(\mathrm{ifft}_2[\tilde{g}(\mathbf{p})\mathrm{fft}_2 S(\mathbf{r})]) \tag{22}$$

for the two approaches, respectively. This was followed by iterative computations. Total error along the centreline was computed after each iteration,

$$\text{Total error} = \sum_{m=1}^{2048} \frac{|\psi_{n+1}(1024, m) - \psi_n(1024, m)|}{|\psi_n(1024, m)|}. \tag{23}$$

The steady-state condition was met, when the error was less than 10^{-4}. If the steady-state condition was not satisfied, $\psi_{\mathrm{TBS}_{n+1}}$ (after multiplying it with *AtnMsk* as defined in Equation (18)) was inserted in Equation (19) as an input to proceed for the next iteration. The same steps were also followed for the CBS method. The complete numerical code is available at [*14*].

4. Results

Figure 2 shows the variation of the pressure field as a function of frequency (7–2000 MHz) for the numerical solution at different speed-of-sound mismatch conditions. The corresponding pressure field provided by the exact method was also plotted for comparison. The variation of the size parameter ($k_f a$) for the entire frequency range was presented on the top (along x-axis) in each figure. These curves exhibit well-known peaks and dips pattern. The number of oscillations increases as v_s was decreased from 1950 to 1200 m/s. Both the TBS and CBS methods exhibit good agreement with the exact result over the entire frequency/size parameter range (see Figure 2(b–e)). The locations and depths of the minima were well reproduced by the TBS and proposed CBS methods as evident from these figures. Figure 2(a,f) displays that the CBS method provides accurate fits to the exact/analytical results. However, TBS curves (scale along the right y-axis) demonstrate large deviation compared to the exact method in Figure 2(a,f), where v_s was 1950 m/s and 1200 m/s, respectively. The difference between TBS and exact/analytical solution is non-linear as the frequency/size parameter increases. The nonlinear behaviour distinctively appears for approximately $k_f a >$ 24 in Figure 2(a) and $k_f a >$ 8.5 in Figure 2(f).

Plots of the error for an example frequency of 505 MHz versus iteration were provided in Figures 3(a–c) with varying speed sound-of-speed in source region. The error for the proposed CBS method gradually decreases as the iteration progresses in all cases, however, the TBS fails to converge when speed-of-sound mismatch is −20 % with respect to that of the surrounding medium (see Figure 3(c)). Even though these plots are specific to frequency of 505 MHz, the same trend was observed with rest frequencies in the range of 7–2000 MHz. The TBS method converged over the entire frequency range for $v_s = 1800, 1650, 1500$ and 1350 m/s (see Figure 2(b–e)), however, did not converge for $v_s = 1950$ m/s when approximately $k_f a > 24$ (i.e. $f > 1160$ MHz) and $v_s = 1200$ m/s with approximately $k_f a > 8.5$ (i.e. $f > 400$ MHz) as also evident from Figure 2(a,f), respectively. Further, the CBS technique was found to converge for all conditions (mismatch in speed-of-sound) and at all frequencies (7–2000 MHz) considered in this study (also refer to Figure 2).

The computational time required was more for the proposed CBS method compared to the TBS method, with maximum difference between them being approximately 20% (for frequency of 2000 MHz, the average execution time of TBS method was 64 sec and proposed CBS method was 77 sec across various v_s values) as the CBS method requires an additional pre-conditioning. As expected the error is much higher in the case of TBS method, when the speed-of-sound mismatch is −20% (Figure 3(c)) even after 500 iterations (consistent with plots in Figure 2(f)).

5. Discussion and conclusions

In this work, for the first time, the Born-series methods were deployed to provide numerical solution to the time-independent PA wave equation, which retains terms originating from acoustic inhomogeneity of the source region. As stated earlier, for finite ϵ, wave number is a complex quantity, background medium becomes lossy and thus, Green's function decays exponentially with distance. Further, in this construct though Green's function decays exponentially with distance but the final solution does not follow the same trend. This is because the scattering potential compensates the attenuation by providing equal amount of gain to the solution. This works for a homogeneous medium as well. The scattering potential even for a homogeneous medium becomes non-zero (i.e. $V = -\mathrm{i}\epsilon$) in this approach.

The TBS and CBS techniques in general can be used to compute solutions for various media with acoustic inhomogeneity of arbitrary shape. The proposed CBS method was shown to be effective compared to TBS scheme especially for cases where the variation of the speed-of-sound of the source region being greater than 22% or less than −11% with respect to the surrounding medium. The CBS algorithm has been developed by utilization of a pre-conditioner (γ) into the TBS scheme, this pre-conditioner compensates for the speed-of-sound

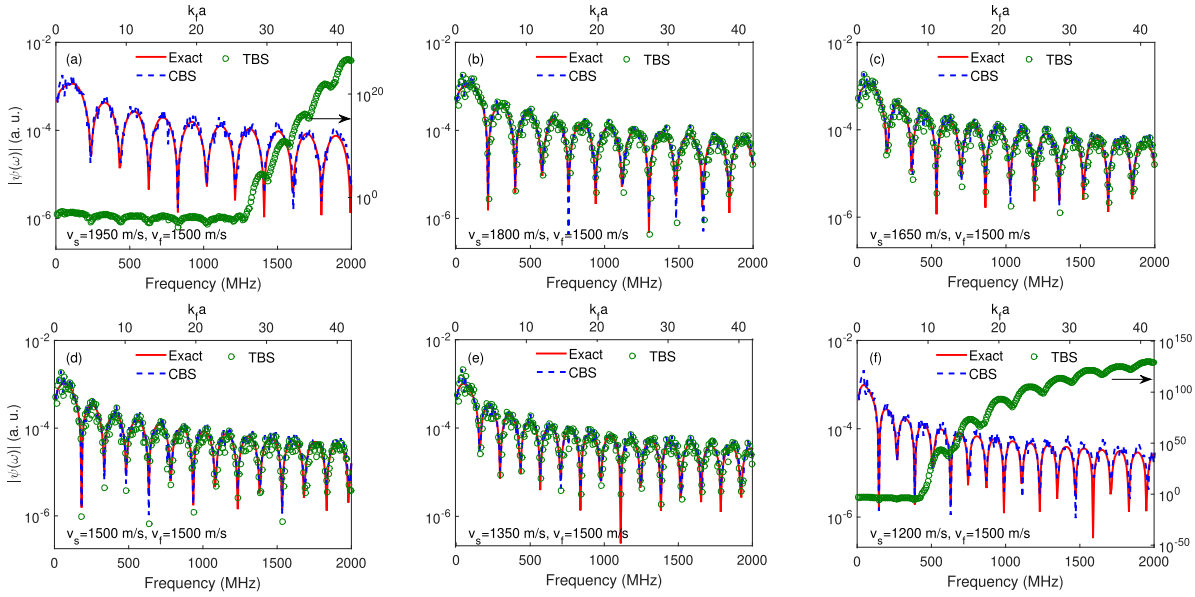

Figure 2. Plots of the pressure field over a frequency range of 7–2000 MHz for exact, TBS, and CBS methods for the media having speed-of-sound as $v_f = 1500$ m/s and the source region v_s as (a) 1950 m/s (b) 1800 m/s, (c) 1650 m/s, (d) 1500 m/s, (e) 1350 m/s, and (f) 1200 m/s. The scale for the PA pressure data for the TBS method is along the right y-axis in (a) and (f). The corresponding values of $k_f a$ are shown on the top (along x-axis).

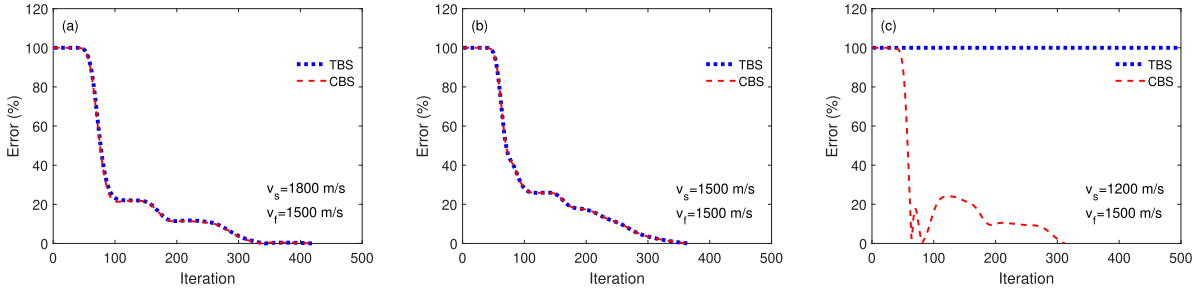

Figure 3. Plot of the error (in %) for an example frequency of 505 MHz utilizing TBS and CBS methods with media speed-of-sound being $v_f = 1500$ m/s and source region v_s as (a) 1800 m/s, (b) 1500 m/s, and (c) 1200 m/s. Error at nth iteration has been obtained as, Error $= (|(|\psi_n| - |\psi_{\text{end}}|)|/|\psi_{\text{end}}|) \times 100\%$, where suffix end indicates the last iteration. For all results, the pressure has been computed at the detector location.

mismatch. Onsabrugge et al. [5] proved that the parameter γ and non-vanishing ϵ ensure convergence of the CBS technique. Further, higher the value of ϵ, greater the attenuation of the pressure wave within the boundary region. The scattering potential ($V(\mathbf{r})$) appearing from the speed-of-sound contrast acts as a potential well when $v_s > v_f$ or $k_s < k_f$. On the other hand, it behaves as a potential barrier when $v_s < v_f$ or $k_s > k_f$.

This work has shown that TBS method provides accurate estimates even for large particles, if the speed-of-sound mismatch lies between approximately 22% and −11% (see Figure 2(b–e)). It also takes less computing time than the proposed CBS approach as the computational complexity is lower in this case. For smaller speed-of-sound mismatch problems, the TBS method can provide a computationally efficient solution. For rest cases, the CBS method is effective and provides quick convergence. The theoretical framework presented here does not include density mismatch between the source and the ambient medium. Therefore, the role of density mismatch on the performance of presented iterative methods (TBS and CBS) needs to be investigated. The theoretical model can be employed to calculate the PA field for a tissue if an ensemble of PA sources can be accommodated within the computational domain. The effect of multiple scattering, arising from speed-of-sound mismatch of the PA sources with respect to the surrounding medium, can also be better investigated using the proposed CBS method.

In conclusion, the Born-series methods are effective in providing accurate solutions for the time-independent PA wave equation. Among the methods presented here,

the CBS method provides a robust approach for incorporating acoustic inhomogeneity of the source region compared to TBS method. It can provide accurate results for arbitrarily large source with sufficiently strong speed-of-sound mismatch (i.e. $\approx$ 30% to $-$20%). Future work includes implementation of parallel computation for calculation of PA signals generated by normal and deformed RBCs in three dimensions.

Acknowledgments

The computational results reported in this work were performed on the Central Computing Facility of IIITA, Allahabad. The authors would like to thank Pankaj Warbal, Deepak Sonker, Ravi Prakash of BMIL, IIITA and Sreedevi Gutta of MIG, IISc for their help.

Disclosure statement

No potential conflict of interest was reported by the author(s).

Funding

No funding was received for this work.

References

[1] Rossum MCWV, Nieuwenhuizen TM. Multiple scattering of classical waves: microscopy, mesoscopy and diffusion. Rev Mod Phys. 1999;71(1):313–371.
[2] Schäfer J, Kienle A. Scattering of light by multiple dielectric cylinders: comparison of radiative transfer and Maxwell theory. Opt Lett. 2008;33(20):2413–15.
[3] Bohren CF, Huffman DR. Absorption and scattering of light by small particles. Weinheim, Germany: Wiley-VCH; 1998.
[4] Morse PM, Feshbach H. Methods of theoretical physics. New York: McGraw-Hill; 1953. p. 791–895.
[5] Osnabrugge G, Leedumrongwatthanakun S, Vellekoop IM. A convergent Born series for solving the inhomogeneous Helmholtz equation in arbitrarily large media. J Comput Phys. 2016;322:113–124.
[6] Krüger B, Brenner T, Kienle A. Solution of the inhomogeneous Maxwell's equations using a Born series. Opt Exp. 2017;21:2165–182.
[7] Diebold GJ, Sun T, Khan MI. Photoacosutic monopole radiation in one, two and three dimensions. Phys Rev Lett. 1991;67(24):3384–3387.
[8] Treeby BE, Cox BT. k-Wave: MATLAB toolbox for the simulation and reconstruction of photoacoustic wave fields. J Biomed Opt. 2010;15(2):021314.
[9] Baddour N. Theory and analysis of frequency-domain photoacoustic tomography. J Acoust Soc Am. 2008;123(5):2577–2590.
[10] Baddour N, Mandelis A. The effect of acoustic impedance on subsurface absorber geometry reconstruction using 1D frequency-domain photoacoustics. Photoacoustics. 2015;3(4):132–142.
[11] Saha RK, Karmakar S, Adhikari A, et al. Photoacoustic field calculation for nonspherical axisymmetric fluid particles. Biomed Phys Eng Exp. 2017;3: 015017.
[12] Kaushik A, Sonker D, Saha RK. Study on angular distribution of differential photoacoustic cross-section and its implication in source size determination. J Opt Soc Am A. 2019;36(3):387–396.
[13] Saha RK, Kolios MC. A simulation study on photoacoustic signals from red blood cells. J Acoust Soc Am. 2011;129(5):2935–2943.
[14] Available from: https://github.com/ratanksaha/Photoacoustic-field-calculation.